Sánchez-Arriaga, G.; García-Villalba, M.; Schmehl, R. (2017). Modeling and dynamics of a two-line kite. *Applied Mathematical Modelling*, vol. 47, pp. 473-486.

DOI: https://doi.org/10.1016/j.apm.2017.03.030

Modelling and dynamics of a two-line kite

G. Sánchez-Arriaga[a], M. García-Villalba[a,*], R. Schmehl[b]

[a] *Bioengineering and Aerospace Engineering Department, Universidad Carlos III de Madrid, Avda de la Universidad 30, 28911, Leganes, Spain*
[b] *Delft University of Technology, Faculty of Aerospace Engineering, Kluyverweg 1, 2629HS Delft, The Netherlands*

Abstract

A mathematical model of a kite connected to the ground by two straight tethers of varying lengths is presented and used to study the traction force generated by kites flying in cross-wind conditions. The equations of motion are obtained by using a Lagrangian formulation, which yields a low-order system of ordinary differential equations free of constraint forces. Two parameters are chosen for the analysis. The first parameter is the wind velocity. The second parameter is one of the stability derivatives of the aerodynamic model: the roll response to the sideslip angle, known also as effective dihedral. This parameter affects significantly the lateral dynamics of the kite. It has been found that when the effective dihedral is below a certain threshold, the kite follows stable periodic trajectories, and naturally flies in cross-wind conditions while generating a high tension along both tethers. This result indicates that kite-based propulsion systems could operate without controlling tether lengths if kite design, including the dihedral and sweep angles, is done appropriately. If both tether lengths are varied out-of-phase and periodically, then kite dynamics can be very complex. The trajectories are chaotic and intermittent for values of the effective dihedral below a certain negative threshold. It is found that tether tensions can be very similar with and without tether length modulation if the parameters of the model are well-chosen. The use of the model for pure traction applications of kites is discussed.

Keywords: `Kite Modeling, Lagrangian Systems, Kite Control`

1. Introduction

Kites have been used for recreational purposes since antiquity and, recently, they have been the subject of intensive research for engineering applications. Several kite scenarios require reaching high tether tensions by flying the kite in cross-wind conditions. One of them is the pulling of cargo ships [1, 2]. Another one is airborne wind energy generation, in which tethered flying devices

*Corresponding author: manuel.garcia-villalba@uc3m.es

are employed to extract the kinetic energy of wind at higher altitudes than conventional wind turbines can reach. A main advantage of the technology is the lower material consumption and smaller environmental footprint. Furthermore, the capacity factor can be significantly larger than that of tower-based turbines because of the stronger and more persistent wind at higher altitude and the adaptability of the tethered energy harvesting system to the wind resource [3, 4, 5]. The two pursued concepts are ground-based energy conversion, in which the traction power of the flying device is converted into electricity by a generator on the ground, and airborne energy conversion by wind turbines mounted on the flying device [6, 7]. Most of the implemented concepts are based on a tethered wing as aerodynamic lifting device. The wing is the equivalent of the wind turbine rotor blade with the crucial difference that the blade is constrained to a rotational motion around the turbine hub while the wing is flown on a certain path required by the specific conversion concept. Most of the implemented airborne wind energy concepts are based on pumping cycles comprising a power-generating reel-out phase and a power-consuming reel-in phase [8]. A low power consumption throughout the reel-in phase needs a depowered kite, i.e., angle of attack control to decrease the aerodynamic force.

To analyze the performance of the kite during reel-out and reel-in phases and to assess the flight dynamic feasibility of a certain trajectory a variety of different modeling approaches have been developed in the past. The type of wing varies from highly flexible membrane wings, without any rigid components, to rigid wings. Flexible membrane wings are controlled by actuation of bridle lines which allows rotation and deformation of the entire wing, while rigid wings are generally steered like aircraft using aerodynamic control surfaces [5]. For an accurate simulation of the kite behavior the complex interaction phenomena between airflow and tensile membrane structure have to be taken into account. Breukels [9] has presented a multibody model of a Leading Edge Inflatable tube kite and its bridle line system in combination with a correlation-based aerodynamic load model to predict aeroelastic phenomena during flight. On the other hand, Bosch et al. [10] has used a finite element model of this kite with the same aerodynamic load model. To avoid the complexity of modeling wing deformation de Groot et al. [11] has combined state reduction with a model identification approach. A different approach has been chosen by Fechner et al. [12] who model the structural behavior of kite, bridle lines and main tether by a particle system interconnected by elastic springs and dampers. The aerodynamic loading is discretized by either a single or three different panels, representing two different levels of detail to the problem of kite aerodynamics.

This work constructs a mathematical model of a kite linked to the ground with two tethers of variable lengths. Two-line kite simulators are specially relevant because they can be applied to airborne wind energy generation with a generator on the ground and also they can be employed for traction applications like pulling cargo ships. Regarding the former, a two-line kite can be steered by varying the line lengths and depowered by entirely releasing one line and retracting the wing in a flagged state using the other line [14]. Two-line kites with movable tip attachment points, as the one shown in Fig. 1, can also be

Figure 1: Two-line kite with rack-and-pinion system to move tip attachments of lines [13]

depowered [13]. Two-line kite models for static [15] and dynamic [16] studies have been reported in the literature. In the latter, the kite was taken as a single point and tether lengths were assumed to be directly related with a lateral angle appearing in the aerodynamic forces. Our dynamic model considers the kite as a rigid body and incorporates self-consistently in the equations the variations of the tether lengths, as discussed below.

The first goal of this work is the development of a mathematical model that can be combined with other tools like periodic orbit and nonlinear optimal control solvers [17]. For these cases, very detailed simulators – as the one cited in the previous paragraph – can be too demanding from a computational point of view. Compact, efficient, and robust models are more convenient for preliminary design phases, which typically require extensive parametric analysis. The second goal is the analysis of kite dynamics in cross-wind conditions that, as shown by the model, can be driven by passive (kite aerodynamic design) and active (tether length modulation) means.

Keeping low the complexity of the simulator requires inevitably to substitute the flexible tethers by inextensible and straight bars. This is a valid approximation if the tether is short enough. However, this approach introduces some difficulties because the kite should satisfy at any instant the constraints imposed by the rigid tethers. If a classical-mechanics formulation is used, then one finds a set of ordinary differential equations, coming from kite dynamics, coupled with a nonlinear set of algebraic equations due to the constraints. Their self-consistent solutions typically involve the implementation of a Newton-Raphson algorithm at each time step during the integration. For these reasons, many kite simulators derived the equations of motion using analytical mechanics (Lagrange formulation)[18, 19, 20, 21, 22]. For ideal constraints, this technique yields a compact and robust set of ordinary differential equations.

The work is organized as follows. Section 2 describes in detail the hypothesis of the model, the coordinate and frames of references used, and the Lagrange equations of a two-line kite. Section 3 shows that, even with constant tether lengths (no control law is implemented), the kite can naturally fly in cross-wind conditions and generate a high tension at the tethers. Section 4 explores kite dynamics and high tensions generation by implementing a periodic control law. The suitability of the model with periodic orbit solvers is shown. Section 5 summarizes the main results and discusses some applications and future works.

2. The kite system model

2.1. Hypotheses and notation

This section presents a compact dynamical model of a kite with two control lines. For convenience, we will make an extensive use of dimensionless variables and some shortenings to improve the legibility of the work. In particular, we will denote with a dot the derivative of any variable, say a, with respect to the dimensionless time $\tau = t\sqrt{g/L_0}$, $\dot{a} = \mathrm{d}a/\mathrm{d}\tau$. Here g is the gravitational acceleration and L_0 the initial length of one of the tethers. For brevity, the sine and cosine of an angle α will be written as $s\alpha$ and $c\alpha$. Most of the lower case and capital letters denote variables without and with dimensions, respectively. The unit vectors that define a frame of reference are denoted as $\boldsymbol{i}_\alpha$, $\boldsymbol{j}_\alpha$ and $\boldsymbol{k}_\alpha$, with α a subscript that identifies the reference frame. We will also make extensive use of rotation matrices that relate the vector components in different basis. For instance, the components of a vector $\boldsymbol{a} = x_E\boldsymbol{i}_E + y_E\boldsymbol{j}_E + z_E\boldsymbol{k}_E = x_1\boldsymbol{i}_1 + y_1\boldsymbol{j}_1 + z_1\boldsymbol{k}_1$ are related by

$$\begin{pmatrix} x_1 \\ y_1 \\ z_1 \end{pmatrix} = \boldsymbol{R}_{1E} \begin{pmatrix} x_E \\ y_E \\ z_E \end{pmatrix}, \tag{1}$$

where $\boldsymbol{R}_{1E}$ is the rotation matrix that relates the components in the frames 1 and E to be defined below.

The model considers a rigid (flexibility effects are ignored) power kite of mass m, surface S, chord c, wingspan b. For convenience we introduce a reference frame, named the body frame S_B, linked to the kite and with origin at its center of mass G. The S_B axes coincide with the principal axes of inertia of the kite at G. Therefore, the moment of inertia tensor of the kite about point G in the body frame is a diagonal matrix. We write it as $\boldsymbol{I}_G = mL_0^2\boldsymbol{\iota}_G$, with $\boldsymbol{\iota}_G$ the dimensionless matrix

$$\boldsymbol{\iota}_G = \begin{pmatrix} \iota_x & 0 & 0 \\ 0 & \iota_y & 0 \\ 0 & 0 & \iota_z \end{pmatrix}. \tag{2}$$

The second hypothesis of the model is related to the physical properties of the tethers. Their inertial, flexibility and elastic effects are ignored. The tethers, taken as rigid massless bars, connect the ground fixed point O_E with the kite

attachment points A^+ and A^- (see Fig. 2). The position vectors of these points with respect to the body frame are

$$\overline{GA}_\pm = L_0 \left(x_A \boldsymbol{i}_B \pm y_A \boldsymbol{j}_B + z_A \boldsymbol{k}_B \right), \tag{3}$$

with x_A, y_A and z_A three dimensionless constants. Unlike the kite shown in Fig. 1, the distances between the center of mass of the kite and the attachment points A^+ and A^- are constant in our model and these points are also symmetric with respect to the plane of symmetry of the kite.

Extending our model to kites with rack-and-pinion control system which move the tip attachments of the bridle lines (see Fig. 1) just requires minor modifications like writing Eq. (3) as $\overline{GA}_\pm = L_0 \left(x_{A\pm} \boldsymbol{i}_B + y_{A\pm} \boldsymbol{j}_B + z_{A\pm} \boldsymbol{k}_B \right)$ and including six additional functions in the control vector ($x_{A\pm}$, $y_{A\pm}$ and $x_{A\pm}$). Such modifications are beyond the scope of this work that is focused on the generation of high tensions for pulling purposes and does not involve any depowered phase. The complex dynamic interaction between the kite-tether system and the system that is pulled, such as a ship or a mobile ground station, may also be considered. For example, when pulling a ship the motion of the ship caused by the waves affects also the flight dynamics of the kite. This is of particular relevance during launching and landing of the kite on the ship, when the deployed tether is short, the kite is close to the ship and the risk of collision is thus high. Such analysis would require the coupling between the present model and the dynamics of the pulled object, a topic that is left for future works.

Our third and last hypothesis involves the wind velocity, whose intensity and direction is constant. This property is used to introduce an inertial frame of reference, named the Earth frame S_E, with origin at point O_E, where the two control lines of the kite meet. The plane spanned by the $O_E x_E$ and $O_E y_E$ axes coincides with the (flat) ground and the $O_E z_E$ axis points downwards to the Earth's center. The $O x_E$ axis is opposed to the wind velocity vector, which can thus be resolved in the reference frame S_E as

$$\boldsymbol{V}_w = -\sqrt{g L_0} v_w \boldsymbol{i}_E, \tag{4}$$

with v_w a given dimensionless and positive quantity that gauges the strength of the wind. Time-dependent wind velocities, ignored in our work, can be incorporated to the model by just giving a law $v_w(\tau)$.

2.2. State and control vectors

In the absence of the constraints, six coordinates are required to describe the motion of a rigid kite, which is kinematically equivalent to the motion of S_B with respect to S_E. However, the two attachment points A_+ and A_- are linked with point O_E by tethers of given lengths $L_{A_+}(t)$ and $L_{A_-}(t)$, respectively. Therefore, due to the constraints, the system has $6 - 2 = 4$ degrees of freedom. The choice of these four coordinates is very important because it affects to the complexity of the resulting set of equations. Figures 2 and 3 provide sketches of

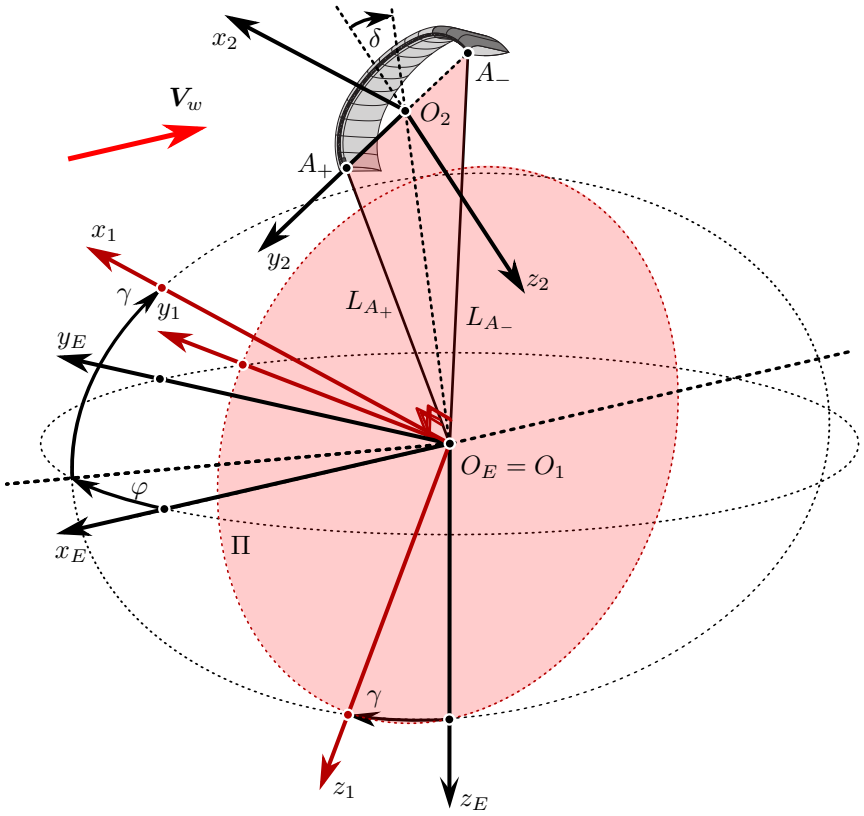

Figure 2: Sketch that shows the position of the kite with respect to the S_E reference frame, the auxiliary reference frames S_1 and S_2 and the definition of the state angles φ and γ and of the control angle δ. The Π plane which is defined by the points O_E, A_+ and A_- is highlighted in red.

the model, including the various reference frames employed and the state and control angles to be defined below.

A key geometrical element of the system is plane Π, defined by the three points O_E, A_+ and A_- (see Fig. 2). For convenience, we introduce an auxiliary reference frame S_1 with origin at $O_E \equiv O_1$ and axes O_1y_1 and O_1z_1 spanning the Π plane. The precise orientation of frames S_1 with respect to S_E is given by two consecutive rotations. The first one is a rotation of value $\varphi(\tau)$ about $\boldsymbol{k}_E$ and the second is a rotation of value $\gamma(\tau)$ about j_1. Therefore, the rotation matrix $\boldsymbol{R}_{1E}$ that transforms vector components from S_E to S_1 is

$$\boldsymbol{R}_{1E} = \begin{pmatrix} c\gamma c\varphi & c\gamma s\varphi & -s\gamma \\ -s\varphi & c\varphi & 0 \\ s\gamma c\varphi & s\gamma s\varphi & c\gamma \end{pmatrix} \tag{5}$$

and the angular velocity of S_1 with respect to S_E reads $\boldsymbol{\Omega}_{1E} = \sqrt{g/L_0}\,(\dot{\varphi}\boldsymbol{k}_E + \dot{\gamma}\boldsymbol{j}_1)$.

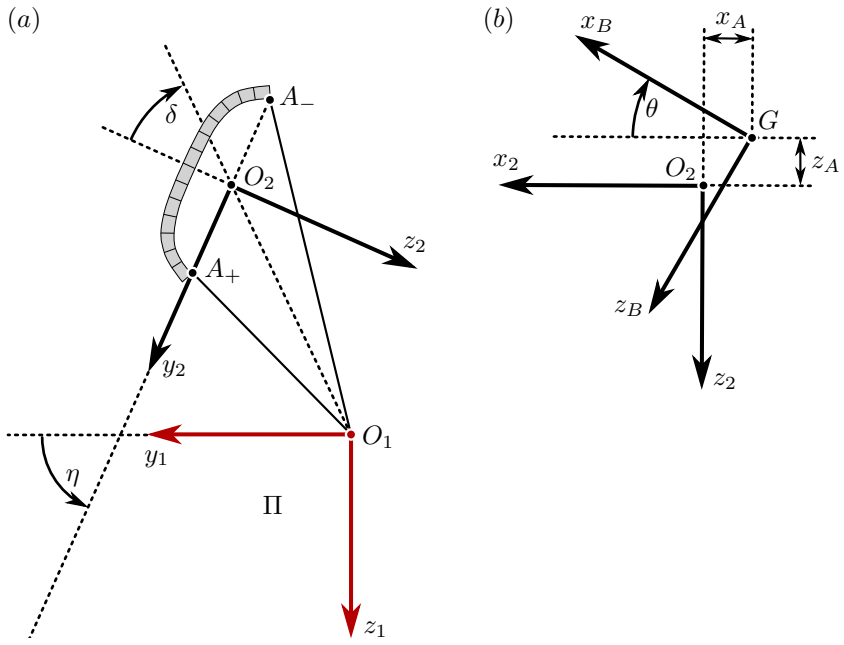

Figure 3: *a*) Sketch of the Π plane including the definition of the state angle η and the control angle δ. *b*) Sketch showing the definition of the state angle θ that relates the intermediate reference frame S_2 and the body reference frame S_B.

Points O_E, A_+ and A_- are the vertices of a triangle. Since its three sides (L_{A_+}(t), $L_{A_-}(t)$ and the constant distance, $2L_0y_A$ between points A_+ and A_-) are known, and one of its vertex coincides with $O_E = O_1$, just one coordinate is needed to place the triangle within Π. For convenience we introduce a reference frame S_2 that moves linked to the triangle (see Figs. 2 and 3*a*). Its origin, O_2, is at the midpoint of the segment $\overline{A_+A_-}$, the O_2y_2 axis is pointing from A_- to A_+, the O_2z_2 axis is contained in the Π plane, and O_2x_2 axis is normal to Π. The relative position of S_2 with respect to S_1 is given by the angle $\eta(\tau)$ between O_1y_1 and O_2y_2. The rotation matrix $\boldsymbol{R}_{21}$, that transforms vector components from S_1 to S_2, is

$$\boldsymbol{R}_{21} = \begin{pmatrix} 1 & 0 & 0 \\ 0 & c\eta & s\eta \\ 0 & -s\eta & c\eta \end{pmatrix} \tag{6}$$

and the angular velocity of S_2 with respect to S_1 is $\boldsymbol{\Omega}_{21} = \sqrt{g/L_0}\dot{\eta}\boldsymbol{i}_2$.

The location of the kite (frame S_B) with respect to S_2 just requires a last additional coordinate. Since the attachment points A_+ and A_- are symmetric with respect to the symmetry plane of the kite, O_2y_2 and O_By_B are also parallel and the orientation of S_2 with respect to S_B is fully determined by the angle

$\theta(\tau)$ between O_2x_B and O_2x_2 (see Fig. 3*b*). The rotation matrix $\boldsymbol{R}_{B2}$ reads

$$\boldsymbol{R}_{B2} = \begin{pmatrix} c\theta & 0 & -s\theta \\ 0 & 1 & 0 \\ s\theta & 0 & c\theta \end{pmatrix} \tag{7}$$

and the angular velocity is $\boldsymbol{\Omega}_{B2} = \sqrt{g/L_0}\dot{\theta}\boldsymbol{j}_B$.

The four angles defined above, that correspond to the four degrees of freedom of the two-line kite system, are gathered in the state vector

$$\boldsymbol{x}_s(\tau) = [\varphi \;\; \gamma \;\; \eta \;\; \theta]^T. \tag{8}$$

Regarding the control vector, a possible choice would be the tether lengths L_{A_+} and L_{A_-}. However, later calculations will show that the distance between points O_E and O_2 and the angle δ between the O_2Z_2 axis and the median of the triangle with vertices O_E, A_+ and A_- (see Fig. 3*a*) will appear naturally in the model. We write the former as $|\overline{O_EO_2}| = L_0\ell(\tau)$, where $\ell(\tau)$ is the dimensionless function

$$\ell(\tau) = \sqrt{\frac{1}{2}\left(\ell_{A_+}^2 + \ell_{A_-}^2 - 2y_A^2\right)}, \tag{9}$$

with $\ell_{A_+} = L_{A_+}/L_0$ and $\ell_{A_-} = L_{A_-}/L_0$. Angle $\delta(\tau)$ is found by applying the law of cosines to the triangle with vertices O_1, O_2 and A_-

$$\delta(\tau) = \arcsin\left[\frac{\ell_{A_+}^2 - \ell_{A_-}^2}{4\ell y_A}\right]. \tag{10}$$

Note that in the particular instant sketched in Fig. 3a, $\ell_{A_-} > \ell_{A_+}$ leading to $\delta < 0$ according to Eq. (10). Both $\ell(\tau)$ and $\delta(\tau)$ are therefore functions of the normalized tether lengths $\ell_{A_+}(\tau)$ and $\ell_{A_-}(\tau)$ and are gathered in the control vector

$$\boldsymbol{x}_c(\tau) = [\ell \;\; \delta]^T. \tag{11}$$

2.3. Lagrangian function and generalized forces

Once the kite state and control vectors are defined, we can write relevant kinematics quantities like the position of the center of mass of the kite with respect to S_E

$$\boldsymbol{R}_G \equiv \overline{O_EG} = \overline{O_EO_2} + \overline{O_2G} = L_0\left\{\ell\left[s\left(\eta+\delta\right)\boldsymbol{j}_1 - c\left(\eta+\delta\right)\boldsymbol{k}_1\right] - \left(x_A\boldsymbol{i}_B + z_A\boldsymbol{k}_B\right)\right\}. \tag{12}$$

The absolute velocity of the center of mass is given by the time rate of change of Eq. (12), $\boldsymbol{V}_G = \mathrm{d}\boldsymbol{R}_G/\mathrm{d}t \equiv \sqrt{gL_0}\boldsymbol{v}_G$. After some algebra, the components of $\boldsymbol{v}_G$ in the body frame can be written as

$$\boldsymbol{v}_G = \boldsymbol{\Upsilon}_s\dot{\boldsymbol{x}}_s + \boldsymbol{\Upsilon}_c\dot{\boldsymbol{x}}_c, \tag{13}$$

with matrices $\boldsymbol{\Upsilon}_s(\boldsymbol{x}_s,\boldsymbol{x}_c)$ and $\boldsymbol{\Upsilon}_c(\boldsymbol{x}_s,\boldsymbol{x}_c)$ given by

$$\boldsymbol{\Upsilon}_s = \begin{pmatrix} \ell\left[s\delta s\gamma s\theta - c\gamma s(\eta+\delta)c\theta\right] - z_A c\gamma s\eta & -\ell c(\eta+\delta)c\theta - z_A c\eta & -\ell s\delta s\theta & \text{-}z_A \\ s\gamma\left(x_A s\theta - z_A c\theta - \ell c\delta\right) - c\gamma c\eta\left(x_A c\theta + z_A s\theta\right) & s\eta(x_A c\theta + z_A s\theta) & \ell c\delta - x_A s\theta + z_A c\theta & 0 \\ -\ell\left[s\delta s\gamma c\theta + c\gamma s(\eta+\delta)s\theta\right] + x_A c\gamma s\eta & -\ell c(\eta+\delta)s\theta + x_A c\eta & \ell s\delta c\theta & x_A \end{pmatrix}, \tag{14}$$

$$\boldsymbol{\Upsilon}_c = \begin{pmatrix} c\delta s\theta & -\ell s\delta s\theta \\ s\delta & \ell c\delta \\ -c\delta c\theta & \ell s\delta c\theta \end{pmatrix}. \tag{15}$$

The absolute angular velocity of the kite is $\boldsymbol{\Omega}_{BE} = \boldsymbol{\Omega}_{B2} + \boldsymbol{\Omega}_{21} + \boldsymbol{\Omega}_{1E} = \sqrt{g/L_0}\left(\dot{\varphi}\boldsymbol{k}_E + \dot{\gamma}\boldsymbol{j}_1 + \dot{\eta}\boldsymbol{i}_2 + \dot{\theta}\boldsymbol{j}_B\right)$. Its components in the body frame are $\boldsymbol{\Omega}_{BE} = P\boldsymbol{i}_B + Q\boldsymbol{j}_B + R\boldsymbol{k}_B \equiv \sqrt{g/L_0}\boldsymbol{\omega}$ with

$$\boldsymbol{\omega} = \begin{pmatrix} -c\gamma c\eta s\theta - s\gamma c\theta & s\eta s\theta & c\theta & 0 \\ c\gamma s\eta & c\eta & 0 & 1 \\ c\gamma c\eta c\theta - s\gamma s\theta & -s\eta c\theta & s\theta & 0 \end{pmatrix} \dot{\boldsymbol{x}}_s \equiv \boldsymbol{\Phi}\dot{\boldsymbol{x}}_s. \tag{16}$$

The dimensionless Lagrangian of the kite,

$$\mathcal{L} = \left(\frac{1}{2}m|\boldsymbol{V}_G|^2 + \frac{1}{2}\boldsymbol{\Omega}_{BE}\cdot\boldsymbol{I}_G\cdot\boldsymbol{\Omega}_{BE} + mg\boldsymbol{R}_G\cdot\boldsymbol{k}_E\right)/mgL_0 \equiv e_k - u_p,$$

involves the normalized kinetic and potential energies of the kite. The former is given by $e_k = (v_G^2 + \frac{1}{2}\boldsymbol{\omega}^T\cdot\boldsymbol{\iota}_G\cdot\boldsymbol{\omega})/2$ or, using Eqs. (13) and (16),

$$e_k(\boldsymbol{x}_s,\boldsymbol{x}_c,\dot{\boldsymbol{x}}_s,\dot{\boldsymbol{x}}_c) = \frac{1}{2}\left(\dot{\boldsymbol{x}}_s^T\cdot\boldsymbol{M}^{(s)}\cdot\dot{\boldsymbol{x}}_s + 2\dot{\boldsymbol{x}}_s^T\cdot\boldsymbol{M}^{sc}\cdot\dot{\boldsymbol{x}}_c + \dot{\boldsymbol{x}}_c^T\cdot\boldsymbol{M}^{(c)}\cdot\dot{\boldsymbol{x}}_c\right), \tag{17}$$

with $\boldsymbol{M}^{(s)} \equiv \boldsymbol{\Upsilon}_s^T\cdot\boldsymbol{\Upsilon}_s + \boldsymbol{\Phi}^T\cdot\boldsymbol{\iota}_G\cdot\boldsymbol{\Phi}$, $\boldsymbol{M}^{(sc)} \equiv \boldsymbol{\Upsilon}_s^T\cdot\boldsymbol{\Upsilon}_c$ and $\boldsymbol{M}^{(c)} \equiv \boldsymbol{\Upsilon}_c^T\cdot\boldsymbol{\Upsilon}_c$. Matrix $\boldsymbol{M}^{(c)}$ takes the very simple form

$$\boldsymbol{M}^{(c)} = \begin{pmatrix} 1 & 0 \\ 0 & \ell^2 \end{pmatrix}. \tag{18}$$

and does not depend on the kite state vector $\boldsymbol{x}_s$. Regarding the potential energy, $u_p(\boldsymbol{x}_s,\boldsymbol{x_c}) = -\boldsymbol{r}_G\cdot\boldsymbol{k}_E$, one finds

$$u_p(\boldsymbol{x}_s,\boldsymbol{x}_c) = \ell c\gamma c\left(\eta+\delta\right) - x_A\left[s\gamma c\theta + c\gamma s\theta c\eta\right] - z_A\left[s\gamma s\theta - c\gamma c\theta c\eta\right]. \tag{19}$$

The aerodynamic force, $\boldsymbol{F}_A \equiv mg\boldsymbol{f}_A$, and its torque about point G, $\boldsymbol{M}_A \equiv mgL_0\boldsymbol{m}_A$, are non-conservative and they should be incorporated to the Lagrange equations through the generalized forces

$$Q_i = \boldsymbol{f}_A\cdot\frac{\partial\boldsymbol{v}_G}{\partial\dot{x}_{si}} + \boldsymbol{m}_A\cdot\frac{\partial\boldsymbol{\omega}}{\partial\dot{x}_{si}}, \qquad i = 1,\ldots,4. \tag{20}$$

These generalized forces depend on the aerodynamic velocity of the kite $\boldsymbol{v}_A = \boldsymbol{v}_G - \boldsymbol{v}_w$, which involves the wind velocity $\boldsymbol{v}_w$ and the kite velocity $\boldsymbol{v}_G$. Since

$\boldsymbol{v}_w$ and $\boldsymbol{v}_G$ are projected in the Earth and the body frames in Eqs. (4) and (13), it is necessary to make a coordinate transformation with the rotation matrix $\boldsymbol{R}_{BE}$ to make the substraction. The aerodynamic force and torque in Eq. (20) are here computed with the following model[23]

$$\boldsymbol{f}_A = \mu v_A^2 \left[(C_{x0} + C_{x\alpha}\alpha)\, \boldsymbol{i}_B + C_{y\beta}\beta \boldsymbol{j}_B + (C_{z0} + C_{z\alpha}\alpha)\, \boldsymbol{k}_B \right], \tag{21}$$

$$\boldsymbol{m}_A = \mu v_A^2 \left[\epsilon_b \left(C_{l\beta}\beta + C_{lp} p \right) \boldsymbol{i}_B + \epsilon_c \left(C_{m0} + C_{m\alpha}\alpha + C_{mq} q \right) \boldsymbol{j}_B + \epsilon_b \left(C_{n\beta}\beta + C_{nr} r \right) \boldsymbol{k}_B \right], \tag{22}$$

where $\mu \equiv \rho S L_0/2m$, $\epsilon_b = b/L_0$, $\epsilon_c = c/L_0$, $p = Pb/2V_T$, $q = Qc/V_T$, $r = Rb/2V_T$, ρ the air density, and V_T a reference velocity that is needed for a proper determination of C_{lp}, C_{mq} and C_{nr}. For the present aerodynamic model this reference velocity is $V_T = 7m/s$. The attack and sideslip angles in Eqs. (21) and (22) are given by

$$\alpha = \arctan\left(\frac{\boldsymbol{v}_A \cdot \boldsymbol{k}_B}{\boldsymbol{v}_A \cdot \boldsymbol{i}_B} \right), \quad \beta = \arcsin\left(\frac{\boldsymbol{v}_A \cdot \boldsymbol{j}_B}{|\boldsymbol{v}_A|} \right). \tag{23}$$

The aerodynamic model provides unrealistic forces for large values of the angle of attack, α and the sideslip angle, β. Therefore, the model is only valid when α is below the stall angle ($\alpha < \alpha_s$) and β is below a given threshold angle ($|\beta| < \beta_{max}$). This model constitutes a first aerodynamic model aimed at a basic investigation of kite dynamics. A more sophisticated description, which is beyond the scope of this work, could be incorporated easily to our simulator by just substituting Eqs. (21)-(22) by empirical or numerical aerodynamic models.

2.4. Equations of motion

Lagrangian formulation yields a very compact form for the equations of motion of the kite. Since our system is holonomic, the constraint forces, i.e., the tensions at the two tethers, do not contribute to the generalized forces. The Lagrangian equations then read

$$\frac{\mathrm{d}}{\mathrm{d}\tau}\left(\frac{\partial \mathcal{L}}{\partial \dot{x}_{si}} \right) - \frac{\partial \mathcal{L}}{\partial x_{si}} = Q_i, \qquad i = 1, \ldots, 4. \tag{24}$$

Using Eqs. (13)-(23) in Eq. (24) yields

$$\begin{aligned} M_{ij}^{(s)} \ddot{x}_{sj} + \left[\frac{\partial M_{ij}^{s}}{\partial x_{sk}} \dot{x}_{sk} + \frac{\partial M_{ij}^{s}}{\partial x_{ck}} \dot{x}_{ck} \right] \dot{x}_{sj} + M_{ij}^{(sc)} \ddot{x}_{cj} + \left[\frac{\partial M_{ij}^{(sc)}}{\partial x_{sk}} \dot{x}_{sk} + \frac{\partial M_{ij}^{(sc)}}{\partial x_{ck}} \dot{x}_{ck} \right] \dot{x}_{cj}, \\ -\frac{1}{2} \left(\frac{\partial M_{jk}^{(s)}}{\partial x_{si}} \dot{x}_{sj} \dot{x}_{sk} + 2 \frac{\partial M_{jk}^{(sc)}}{\partial x_{si}} \dot{x}_{sj} \dot{x}_{ck} \right) + \frac{\partial u_p}{\partial x_{si}} = f_{Ak} \Upsilon_{ski} + m_{Ak} \Phi_{ki}, \end{aligned} \tag{25}$$

where we used Einstein summation convention. Note that the term proportional to $\partial M_{jk}^{c}/\partial x_{si}$ is zero because, according to Eq. (18), matrix $\boldsymbol{M}^c$ does not depend on the state vector.

For convenience, we introduce the extended state vector

$$\boldsymbol{u} = [\boldsymbol{x}_s \quad \dot{\boldsymbol{x}}_s], \tag{26}$$

and write Eq. (25) as a system of first order ordinary differential equations

$$\frac{d\boldsymbol{u}}{d\tau} = \boldsymbol{f}\left(\boldsymbol{u}, \tau; \boldsymbol{p}\right). \tag{27}$$

In general, the system is non-autonomous because τ appears explicitly in the right hand side of Eq. (27) due to the control law $\boldsymbol{x}_c$ and its derivatives. Vector $\boldsymbol{p}$ in Eq. (27) gathers all the dimensionless parameters of the model. A summary of the values used in our simulations is given in Table 1. An example of physical parameters yielding the values of Table 1 is $\rho = 1.225 kg/m^3$, $g = 9.8 m/s^2$, $m = 4kg$, $c = 1.5$, $b = 5.8m$, $S = 14.38m^2$. In the next two sections, these parameters were used to provide some results with dimensions and ease the physical understanding. However, the results can be applied directly to kites and tethers of different sizes and lengths if the scaling preserves the dimensionless parameters of Table 1. Note also that y_A does not appear in $\boldsymbol{p}$ thanks to our choice of the control variables $\delta(t)$ and $\ell(t)$. However, this parameter is needed if one wishes to recover the normalized tether lengths ℓ_{A_+} and ℓ_{A_-} from $\delta(t)$ and $\ell(t)$.

Our model is valid for any rigid body towed to the ground by two tethers. A large number of cases, like acrobatic kites, power kites, and aircraft-like kites, could be simulated. The particular shape of the body enters in the model through the value of the aerodynamic coefficients and through the values of the normalized moments of inertia. As shown in Table 1, this work analyzes a power kite and uses the same values of Ref. [22] (see references therein for more details). Parametric studies varying the wind velocity and the stability derivative $C_{l\beta}$ are presented in the following. The motivation behind the selection of this particular stability derivative for the parametric study will become clear in Secs. 3 and 4. $C_{l\beta}$ affects severely to the lateral dynamics of the system and, since it is influenced by the dihedral and the sweep angles [23], it can be tuned by making an appropriate design of the kite. While in aircraft aerodynamics the stability derivatives are often well characterized, the data for kite aerodynamics is scarce. Vortex-lattice method calculations applied to a surf kite provided a value of $C_{l\beta} = -0.49$ [24]. Data for parafoils (which may behave similar as kites) are also available, for example [25] reports $C_{l\beta} = -0.037$.

2.5. Limitations and verification of the model

Given a parameter vector $\boldsymbol{p}$, control laws $\boldsymbol{x}_c$, $\dot{\boldsymbol{x}}_c$ and $\ddot{\boldsymbol{x}}_c$, and a set of initial conditions $\boldsymbol{u}(\tau = 0)$, Eq. (27) can be integrated numerically to find the kite trajectory $\boldsymbol{u}(\tau)$. However, although such an orbit is mathematically correct, it should satisfy a set of conditions to be valid from a physical point of view. First, the two tethers should be under traction at any instant. In order to check this condition, tension forces applied to the kite at points $A_\pm$, $\boldsymbol{T}_\pm(\tau) = mgt_\pm \boldsymbol{u}_\pm$

Symbol	Value	Symbol	Value
ϵ_c	0.0075	ϵ_b	0.029
x_A	0.0037	i_x	1.32×10^{-4}
y_A	0.0145	i_y	2.92×10^{-5}
z_A	0.01	i_z	1.12×10^{-4}
μ	440.4	β_{max}	15°
α_s	25°	v_w	–
C_{x0}	-0.065	$C_{x\alpha}$	0.176
$C_{l\beta}$	–	C_{lp}	-0.15
$C_{y\beta}$	-1.57	C_{m0}	0.1332
$C_{m\alpha}$	-0.7633	C_{mq}	-0.165
C_{z0}	0.116	$C_{z\alpha}$	-2.97
$C_{n\beta}$	-0.027	C_{nr}	-0.002

Table 1: Dimensionless parametera used in the simulations. The stability derivative $C_{l\beta}$ and the normalized wind velocity v_w are used as bifurcation parameters in the analysis.

with $\boldsymbol{u}_\pm \equiv \overline{A_\pm O_E}/|\overline{A_\pm O_E}|$, should be computed from the trajectory $\boldsymbol{u}(\tau)$. The dot products of the unit vectors $\boldsymbol{u}_\pm$ and Newton's Second Law

$$\dot{\boldsymbol{v}}_G = \boldsymbol{k}_E + \boldsymbol{f}_A + t_+\boldsymbol{u}_+ + t_-\boldsymbol{u}_-, \tag{28}$$

yield a couple of equations for the normalized tensions $t_\pm(\tau)$. Note that $\dot{\boldsymbol{v}}_G$ is found from the trajectory $\boldsymbol{u}(\tau)$ by just taking the derivative of Eq. (13) and using Eq. (25). A physically valid trajectory should verify $t_\pm(\tau) > 0, \forall\tau$. In addition, some quantities should be also within certain ranges. The aerodynamic model given by Eqs. (21)-(22) is valid for angles of attack below stall, $\alpha(\tau) < \alpha_s$, and the modulus of the sideslip angle below certain maximum, $|\beta(\tau)| < \beta_{max}$. Finally, the kite should be inside the wind window, $\boldsymbol{R}_G \cdot \boldsymbol{i}_E < 0$ and $\boldsymbol{R}_G \cdot \boldsymbol{k}_E < 0$ $\forall\tau$. The results presented in this paper satisfy all these conditions.

The correct implementation of the simulator has been checked by writing a separate code that solves the differential-algebraic system of equations that results from the classical Newton-Euler equations for the rigid body together with the constraints of the tethers. We took several arbitrary initial conditions and integrated the equations of motion by using the *Lagrangian* and the *classical* codes. They provided the same trajectories up to the error of the numerical integrators. However, the set of differential equations obtained by using the Lagrangian formulation is more appropriate to make complex calculations like the determination of periodic orbits and their stability, and, in addition, its solution is computationally less demanding.

3. Dynamics of the kite with constant tethers lengths.

This section shows that a two-line kite can fly in cross-wind conditions in a stable way without implementing any type of control strategy. Since such a

configuration is very simple and robust, it is an interesting case with applications to wind power generation or pulling boats to save fuel. As shown below, a deep understanding of the kite dynamics and the relevant kite design parameters requires first a discussion of the existence and stability of some families of solutions.

3.1. Kite equilibrium

Under steady wind conditions (v_w is constant) and steady symmetric control laws ($\boldsymbol{x}_c = [\sqrt{1-y_A^2} \;\; 0]^T$), the system admits a symmetric equilibrium state, i.e. a kite state, $\boldsymbol{u}(\tau) = \boldsymbol{u}^*$ that makes $\boldsymbol{f}(\boldsymbol{u}^*) = 0$. Such a condition is verified by a state vector of the form $\boldsymbol{x}_s^* = [0 \;\; \gamma^* \;\; 0 \;\; \theta^*]$, where γ^* and θ^* are constants ($\dot{\boldsymbol{x}}_s = 0$). Substituting this state vector in Eq. (27), yields two coupled nonlinear algebraic equations for γ^* and θ^*. After some algebra, an equation for the equilibrium angle of attack $\alpha^* = \gamma^* + \theta^*$ is found

$$\Lambda\left(x_A \cos\alpha^* + z_A \sin\alpha^*\right) + \epsilon_c\left(C_{m0} + C_{m\alpha}\alpha^*\right) - z_A\left(C_{x0} + C_{x\alpha}\alpha^*\right) + x_A\left(C_{z0} + C_{z\alpha}\alpha^*\right) = 0, \tag{29}$$

where we introduced the parameter $\Lambda \equiv \frac{1}{\mu v_w^2} = \frac{2mg}{\rho S V_w^2}$, which gauges the weight of the kite and the strength of the aerodynamic force. Once α^* is known, θ^* is found from

$$\Lambda \sin(\alpha^* - \theta^*) - \cos\theta^*\left(C_{x0} + C_{x\alpha}\alpha^*\right) - \sin\theta^*\left(C_{z0} + C_{z\alpha}\alpha^*\right) = 0, \tag{30}$$

and γ^* is found from the relation $\gamma^* = \alpha^* - \theta^*$. As shown by Eqs. (29)-(30) the state vector of the symmetric equilibrium is not affected by lateral-directional parameters like $C_{l\beta}$.

The stability of the equilibria, an important feature for kite applications, is investigated by adding a small perturbation $\boldsymbol{u}_1$ to the steady state, substituting $\boldsymbol{u}(\tau) = \boldsymbol{u}^* + \boldsymbol{u}_1(\tau)$ in Sys. (27), and dropping high order terms. One finds the linear system $d\boldsymbol{u}_1/d\tau = \boldsymbol{J}\,|_{\boldsymbol{u}^*}\,\boldsymbol{u}_1$ with $\boldsymbol{J}\,|_{\boldsymbol{u}^*}$ the Jacobian matrix of the flux $\boldsymbol{f}$ evaluated at the equilibrium state. This linear system admits solutions of the type $\boldsymbol{u}_1(\tau) \propto e^{\lambda\tau}$, being the equilibrium state $\boldsymbol{u}^*$ asymptotically stable if all the eigenvalues of $\boldsymbol{J}\,|_{\boldsymbol{u}^*}$ have negative real part.

Thanks to the selection of the coordinates and the aerodynamic model used in our analysis, the motions of the longitudinal (γ_1,θ_1) and lateral-directional (φ_1, η_1) perturbations close to the symmetric equilibrium state are decoupled, as in conventional aircraft flight mechanics[23]. Despite the fact that the symmetric equilibrium position does not depend on lateral-directional parameters, we have observed that its stability does depend on lateral-directional parameters like $C_{l\beta}$. A parametric survey (not shown in this work) varying the tether lengths, the wind velocity and some of the stability derivatives revealed that the symmetric equilibrium of the kite is longitudinally stable. However, it can develop an interesting lateral-directional instability within certain domain of the $C_{l\beta} - v_w$ plane that yields stable periodic orbits with interesting applications like pulling cargo ships. For this reason we finally selected $C_{l\beta}$ and v_w as bifurcation parameters in this work.

Let us first discuss the behavior of the kite for wind velocity equal to $10m/s$. Figure 4 shows the altitude of the kite (top panel) and the side slip angle (bottom panel) as a function of $C_{l\beta}$. We have identified a symmetric steady state which does not depend on $C_{l\beta}$. However, as it will be shown below, its stability does depend on $C_{l\beta}$, and the steady state is stable between two limiting values $(C_{l\beta,min}, C_{l\beta,max})$. When $C_{l\beta}$ is larger than $C_{l\beta,max}$ we have identified a pair of asymmetric steady states. As $C_{l\beta}$ increases, the kite height for these asymmetric steady states quickly decreases and for $C_{l\beta} \sim 0.126$, the kite touches the ground. Note that the sideslip angle is always small remaining below $1.5°$. When $C_{l\beta}$ is smaller than $C_{l\beta,min}$ no additional steady state has been found. Instead, as discussed below, periodic orbits are observed in this range. Note that since the altitude and the sideslip angle of the kite depend on time for these periodic orbits, we plotted their minimum and maximum values in Fig. 4. The existence of an upper boundary, $C_{l\beta,max}$, is not unexpected. It is well-known from conventional aircraft stability analysis that a stable *spiral* mode basically requires a low enough $C_{l\beta}$[23]. Design means like wings with positive dihedral angles and backward sweep angle are normally used to achieve this goal for aircraft. The physical explanation of the lower stability boundary, $C_{l\beta,min}$, is more complex because it involves the tension forces introduced by the two constraints. A kite design with a very low $C_{l\beta}$ does not yield a stable kite equilibrium, but periodic orbits instead.

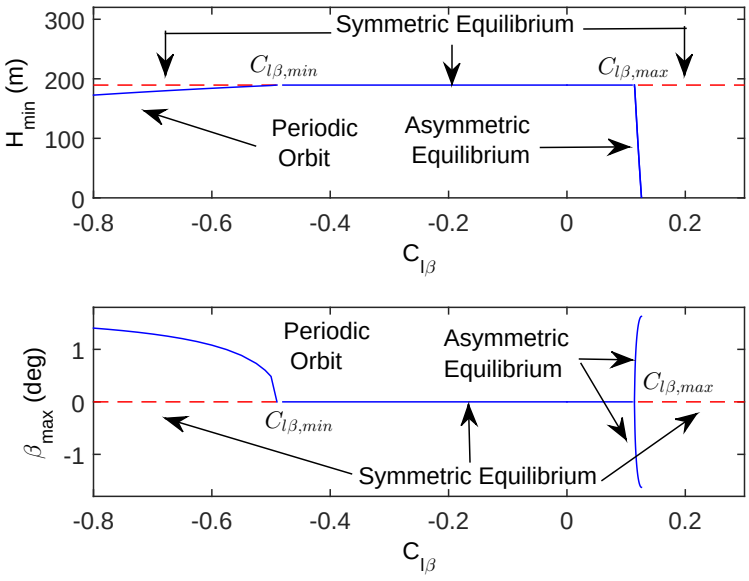

Figure 4: Minimum altitude (top) and maximum sideslip angle (bottom) versus $C_{l\beta}$ for wind velocity equal to $10m/s$. Solid (dashed) lines denote stable (unstable) kite trajectories.

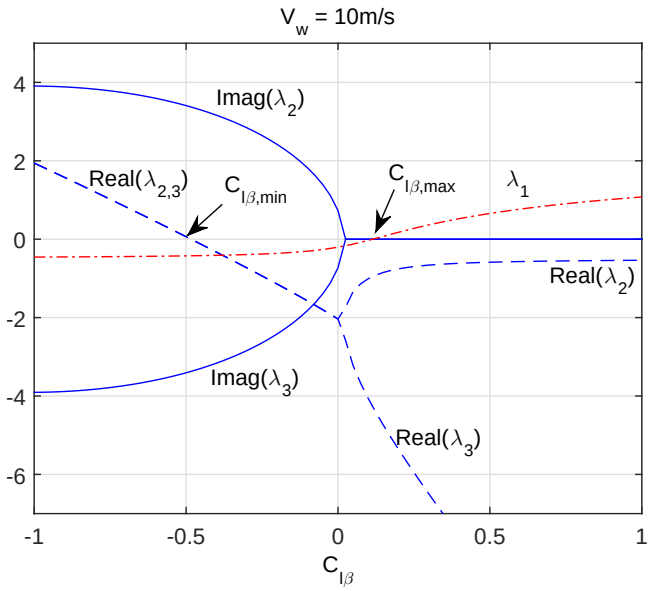

Figure 5: Relevant lateral-directional eigenvalues of $\boldsymbol{J}\,|_{\boldsymbol{u}^*}$ for wind velocity equal to $10m/s$.

In order to determine the stability of these steady state solutions, Figure 5 shows the three relevant lateral-directional eigenvalues of $\boldsymbol{J}\,|_{\boldsymbol{u}^*}$ for wind velocity equal to $10m/s$. The fourth eigenvalue, which is real and negative in the full studied $C_{l\beta}$-range, does not play any role on the bifurcation scenario. For $C_{l\beta} > C_{l\beta,max}$ the symmetric steady state is unstable because λ_1 is real and positive. At $C_{l\beta} = C_{l\beta,max}$ its sign changes through a supercritical pitchfork bifurcation leading to the pair of asymmetric stable equilibria. On the other hand, for $C_{l\beta} < C_{l\beta,min}$, the symmetric equilibrium is unstable because the real part of a pair of complex conjugate eigenvalues (λ_2 and λ_3) becomes positive. The symmetric equilibrium goes through a Hopf bifurcation leading to the branch of periodic orbits mentioned above for $C_{l\beta} < C_{l\beta,min}$. Numerical evidence in Sec. 3.2 shows that the Hopf bifurcation is supercritical and the family of periodic orbits is stable (see Floquet multipliers in Fig. 8).

All the previous results correspond to a wind velocity equal to 10 m/s. The same analysis varying this parameter allows to determine the various regimes of operation of the kite in the $V_w - C_{l\beta}$ plane (see Fig. 6). For wind velocity below certain threshold, no equilibrium exists because the kite stalls. For higher V_w, the kite performs a periodic motion if $C_{l\beta} < C_{l\beta,min}$, stays in a symmetric steady state if $C_{l\beta,min} < C_{l\beta} < C_{l\beta,max}$, and stays in an asymmetric steady state if $C_{l\beta} > C_{l\beta,max}$. As discussed before, the latter only occurs if $C_{l\beta}$ is higher but close to $C_{l\beta,max}$ (otherwise the kite crashes). These results show that lateral instabilities of kites, which have been already found for systems with only one tether [19, 21], can also happen for two-line kites.

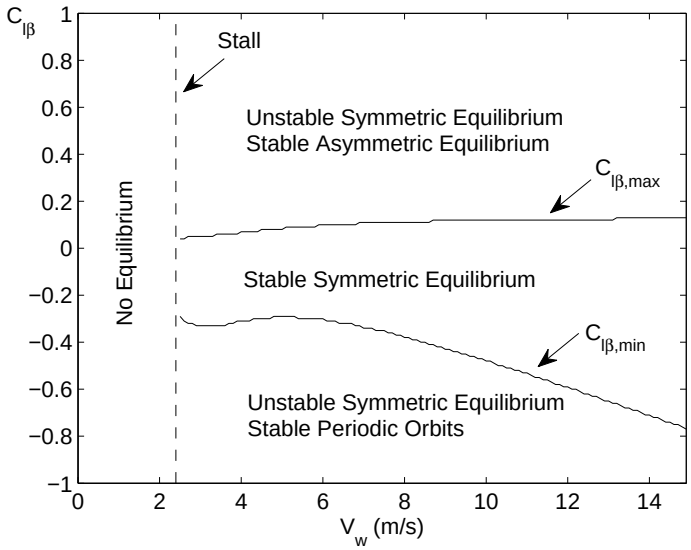

Figure 6: Stability of the kite equilibrium versus the wind velocity and $C_{l\beta}$.

3.2. Cross-wind flight with constant tether lengths

The family of periodic orbits found in Sec. 3.1 has a high interest for certain applications. The top panel in Fig. 7 shows the evolution of the angles φ and γ for periodic orbits with wind velocity equal to 10 m/s and several $C_{l\beta}$ values. The kite describes eight-like trajectories and, as $C_{l\beta}$ decreases moving apart from the Hopf bifurcation point, the amplitude of the lateral motions increases and the period decreases (see bottom panel in Fig. 7). As a result, the aerodynamic velocity and the tension force at the tether are enhanced as $C_{l\beta}$ decreases. This feature of the family of periodic orbits, which yields a kite trajectory flying at cross-wind conditions, can be used to generate power or to pull large boats to save fuel.

The periodic orbits presented in Fig. 7 were computed with a predictor-corrector algorithm that also provides the eigenvalues ζ_j of the monodromy matrix [26]. Floquet theory states that a periodic orbit is stable if all these eigenvalues have moduli less or equal to one. Note that, since the system is autonomous, there is an eigenvalue with value +1. The stability is studied by plotting the eigenvalues in the complex plane and the unit circle. As shown by Fig. 8 all the eigenvalues are within the circle and the family of periodic orbits is stable (the Hopf bifurcation is supercritical). However, as $C_{l\beta}$ decreases there is a pair of complex conjugated eigenvalues that approaches to the stability boundary. This could lead to a new family of solutions, probably quasi-periodic. In any case, we did not explore such a limit regime because physically valid periodic orbits do not exist for arbitrarily small $C_{l\beta}$. As shown in the top panel

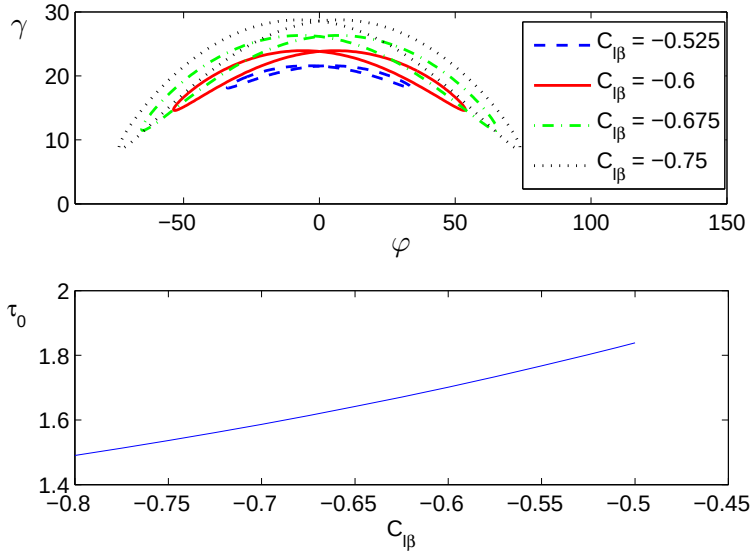

Figure 7: $\varphi - \gamma$ trajectories of periodic orbits for several $C_{l\beta}$ values (top) and normalized orbit periods versus $C_{l\beta}$ (bottom). Both panels correspond to a wind velocity of 10 m/s.

of Fig. 7, the minimum of the elevation γ goes to zero as $C_{l\beta}$ decreases and, at some point the kite leaves the wind window.

Figures 6 and 7 show that the kite can naturally fly in cross-wind conditions within a wide range of wind conditions if it is designed with $C_{l\beta} < C_{l\beta,min}$. This is interesting because, as it is well-known [6], the tether tension is much higher in cross-wind conditions than in a steady state. In order to assess quantitatively this tension gain we computed the modulus of the normalized average tension in one kite loop

$$\langle t \rangle = \frac{1}{\tau_0} \int_0^{\tau_0} (|\boldsymbol{t}_+| + |\boldsymbol{t}_-|)\, \mathrm{d}\tau. \tag{31}$$

Figure 9 shows that a kite following a periodic orbit can produce a tension that is a factor 2.5 larger than the one reached in steady conditions. Since the periodic orbits are stable and they do not involve any type of control (open or closed), these kite trajectories are good candidates to produce high traction in a robust way.

4. Dynamics of the kite with periodically-varying tethers lengths.

We now explore the dynamics when tether lengths are varied following a simple control law. The control variable ℓ in Eq. (11) is kept constant and the angle δ is varied according to

$$\delta(\tau) = \delta_0 \sin \omega_\delta \tau, \tag{32}$$

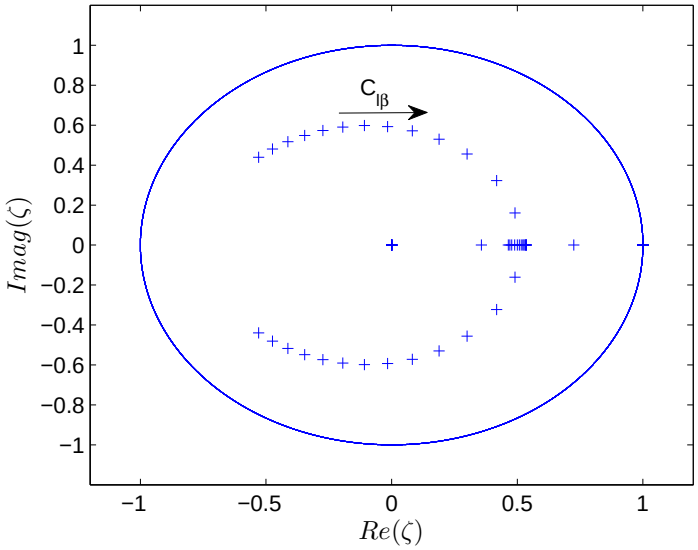

Figure 8: Loci of the eigenvalues of the monodromy matrix in the complex plane when varying $C_{l\beta}$, for wind velocity equal to 10 m/s.

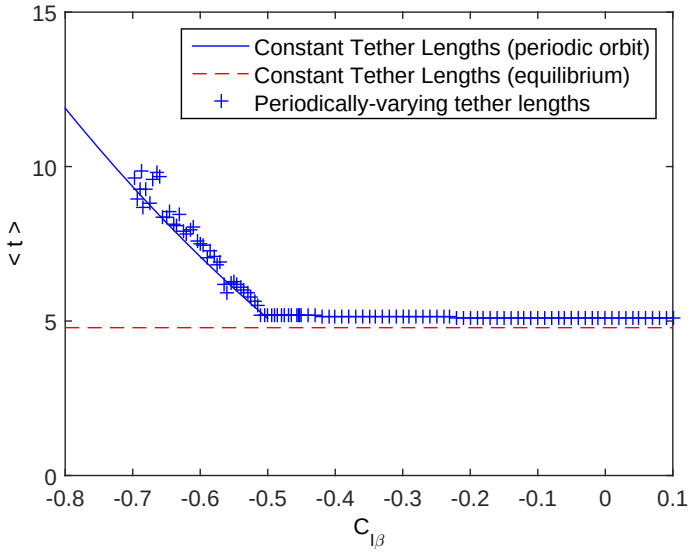

Figure 9: Normalized average tension versus $C_{l\beta}$ for wind velocity equal to $10m/s$.

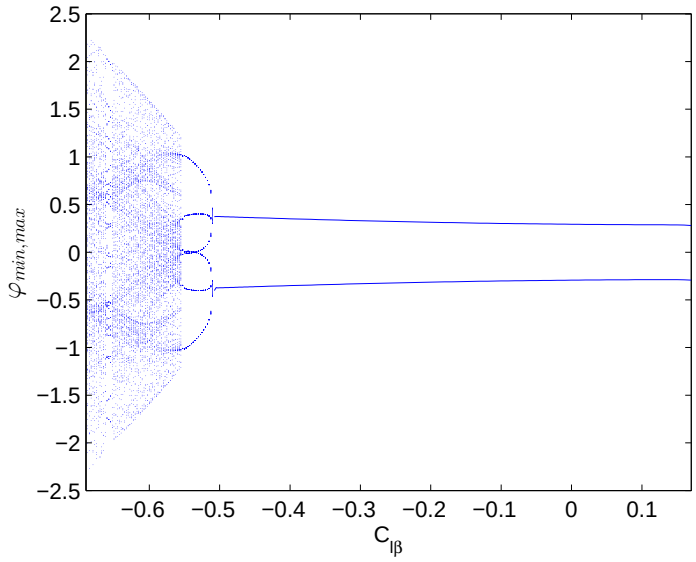

Figure 10: Bifurcation diagram with periodically-varying tethers lengths.

where δ_0 and ω_δ are two constants. This control law reels in and out the right and left tether periodically, thus driving a lateral motion of the kite. For this special case, Sys. (25) is non-autonomous and one would expect, in principle, the existence of periodic orbits with period equal to an integer multiple of $2\pi/\omega_\delta$. However, as shown below and depending on the aerodynamic properties of the kite, the dynamics can be much more complex than regular periodic motions. Hereafter we set $\delta_0 = \pi/20$, $\omega_\delta = 10$, and $V_w = 10m/s$. The results are summarized in Fig. 10 that shows a bifurcation diagram of the extremes of φ versus $C_{l\beta}$. For each value of $C_{l\beta}$, the trajectory was computed by integrating Sys. (25) numerically and, after a sufficiently long transient time, the relative extremes of φ (maxima and minima) were recorded.

For values of $C_{l\beta}$ within the range $-0.51 \leq C_{l\beta} \leq 0.17$ the orbits are periodic and stable. In one period, the lateral angle φ reaches a maximum and a minimum, which appear in the bifurcation diagram as a couple of branches (see Fig. 10). An example is given in panel (a) of Fig. 11 that shows the kite trajectory with $C_{l\beta} = -0.3$. For $C_{l\beta} \approx 0.17$ and $C_{l\beta} \approx -0.51$ the branch of periodic orbits becomes unstable. A detailed stability analysis reveals that a real eigenvalue of the Monodromy matrix leaves the unit circle at $C_{l\beta} \approx 0.17$ and, at the bifurcation point $C_{l\beta} \approx -0.51$, a pair of complex conjugate eigenvalues also leave the unit circle. These two bifurcations limit the allowable $C_{l\beta}$-range with stable periodic orbits.

For $C_{l\beta} < -0.51$ the behavior of the kite is more complex. As compared with the typical eight-like orbit with $C_{l\beta} = -0.3$ in Panel (a) of Fig. 11,

decreasing $C_{l\beta}$ gives rise to lateral oscillations of much higher amplitude and a kite flight at lower altitude (see trajectory in Panel (a) with $C_{l\beta} = -0.54$). At $C_{l\beta} = -0.55$ the model predicts a crisis and the appearance of a chaotic attractor for $C_{l\beta} < -0.55$. The bifurcation diagram in Fig. 10 and the orbit in Panel (b) of Fig. 11 with $C_{l\beta} = 0.6$ also show intermittency. The kite spends most of the time close to an unstable periodic orbit and makes excursions to higher altitudes before being re-injected again to the neighborhood of the periodic orbit.

Figure 9 shows the normalized average tension for the solutions displayed in Fig. 10. For the chaotic trajectories, the tensions were averaged during a time $20 \times 2\pi/\omega_\delta$. The tensions at the tethers for the periodic orbits ($C_{l\beta} > -0.51$) are low and close to the one provided by the kite in equilibrium if tether lengths are kept constant. This is in agreement with the small amplitudes of the lateral motions observed in panel (a) of Fig. 11. For low $C_{l\beta}$ values, when the dynamics is chaotic, the tensions are much higher and similar to the ones found for the periodic orbits of Sec. 3. Therefore, a simple solution to achieve high tension is: (i) keep both tethers with equal and constant lengths, and (ii) make a kite design with a $C_{l\beta}$ that yields natural periodic orbits.

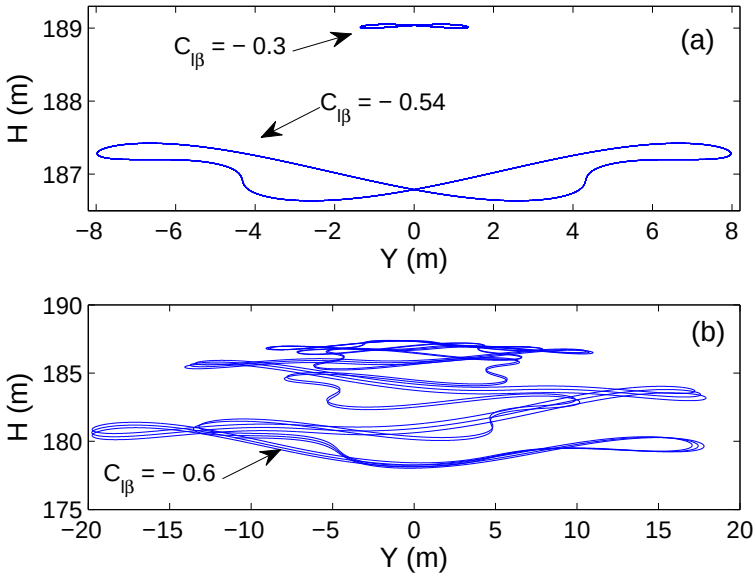

Figure 11: Kite trajectories in a vertical plane perpendicular to the wind direction for three $C_{l\beta}$ values. (a) $C_{l\beta} = -0.3, -0.54$. (b) $C_{l\beta} = -0.6$.

5. Conclusions

Kite modeling and the implementation of efficient flight simulators are necessary to investigate potential applications and the viability of this technology. This work shows that Lagrange formulation, which allows to get rid of the constraint forces (tether tensions) in the equation of motions, is a good choice to simulate kites linked to the Earth by two rigid tethers. Comparisons with another in-house simulator based on a classical formulation, which has been used to double-check all the results of this work, shows a noticeable gain in terms of speed and robustness. The low dimension of the model, the state vector has just dimension four, makes it suitable to be used in more complex scenarios like in nonlinear optimal control problems or the periodic orbit solver used in our analysis. A second feature of the model is its modularity. For example, if a more accurate aerodynamic model is available from experimental measurements or computational fluid dynamic simulations, it can be easily incorporated to the current simulator by just changing accordingly the generalized forces.

The model shows that parameter $C_{l\beta}$ should belong to a certain range, which depends on the wind velocity, to make the steady and symmetric flight of the kite stable. Even more interestingly, if $C_{l\beta}$ is below a threshold, then the kite naturally flies in cross-wind conditions periodically and produces a relatively high tension force at the ground attachment point. Such a manouver, which is simple and robust because it does not involve active control and it is naturally stable, is an interesting operational state to be investigated further in the future. If tether lengths are varied periodically in time, then kite dynamics is highly affected by the value of $C_{l\beta}$. The model exhibits an interesting set of bifurcations and solutions that, beyond its mathematical interest, have consequences for kite system design. For small $C_{l\beta}$ we found that the amplitude of the lateral oscillations of the kite are high and the motion can be chaotic. The kite flies in cross-wind conditions and the tensions generated in the tethers are highly dependent on the choice of $C_{l\beta}$. Therefore, kite aerodynamic design is crucial to achieve the desired conditions.

Besides giving insight of the flight mechanics of kites, the model can be applied to the investigations of the reel-out phase in airborne wind energy generation scenarios and cargo ship pulling by power kites. The case of the reel-in phase simulation would be more problematic because the model cannot simulate a flagging manoeuver or a time dependent location of the attachment points. The latter could be addressed without major modifications by just adding more variables to the control vector while taken into account the time-dependence of the coordinates of the attachments points. Another interesting extension of the model is the simulation of kites with four lines, like the ones used in kitesurf. Since adding two straight and inextensible tethers would make the problem hyperstatic, elasticity effects should be included for the two additional tethers. The model presented in this work could be kept as it is, but just adding the contribution to Q_i of the tension forces provided by the extensible tethers. Further work in this direction is in progress.

Acknowledgments

This work was supported by the Ministerio de Economía y Competitividad of Spain and the European Regional Development Fund under the project ENE2015-69937-R (MINECO/FEDER, UE). GSA work is supported by the Ministerio de Economía y Competitividad of Spain under the Grant RYC-2014-15357. MGV was partially supported by grant TRA2013-41103-P (MINECO/FEDER, UE). RS was partially supported by the projects AWESCO (H2020-ITN-642682) and REACH (H2020-FTIPilot-691173).

References

[1] M. Erhard, H. Strauch, Control of towing kites for seagoing vessels, IEEE T. Contr. Syst. T. 21 (5) (2013) 1629–1640. arXiv:1202.3641, doi:10.1109/TCST.2012.2221093.

[2] M. Erhard, G. Horn, M. Diehl, A quaternion-based model for optimal control of the SkySails airborne wind energy system, ZAMM J. Appl. Math. Mech.arXiv:1508.05494, doi:10.1002/zamm.201500180.

[3] C. L. Archer, An introduction to meteorology for airborne wind energy, in: U. Ahrens, M. Diehl, R. Schmehl (Eds.), Airborne Wind Energy, Green Energy and Technology, Springer, Berlin Heidelberg, 2013, Ch. 5, pp. 81–94. doi:10.1007/978-3-642-39965-7_5.

[4] J. Heilmann, C. Houle, Economics of pumping kite generators, in: U. Ahrens, M. Diehl, R. Schmehl (Eds.), Airborne Wind Energy, Green Energy and Technology, Springer, Berlin Heidelberg, 2013, Ch. 15, pp. 271–284. doi:10.1007/978-3-642-39965-7_15.

[5] A. Cherubini, A. Papini, R. Vertechy, M. Fontana, Airborne wind energy systems: A review of the technologies, Renew. Sustainable Energy Rev. 51 (2015) 1461–1476. doi:10.1016/j.rser.2015.07.053.

[6] M. L. Loyd, Crosswind kite power, J. Energy 4 (3) (1980) 24–30. doi:10.2514/3.48021.

[7] U. Ahrens, M. Diehl, R. Schmehl (Eds.), Airborne Wind Energy, Green Energy and Technology, Springer, Berlin Heidelberg, 2013. doi:10.1007/978-3-642-39965-7.

[8] R. Schmehl (Ed.), Book of Abstracts Int. Airborne Wind Energy Conf. 2015, Delft University of Technology, Delft, The Netherlands, 2015. doi:10.4233/uuid:7df59b79-2c6b-4e30-bd58-8454f493bb09.

[9] J. Breukels, An engineering methodology for kite design, Ph.D. thesis, Delft University of Technology (2011).
URL http://resolver.tudelft.nl/uuid:cdece38a-1f13-47cc-b277-ed64fdda7cdf

[10] A. Bosch, R. Schmehl, P. Tiso, D. Rixen, Dynamic nonlinear aeroelastic model of a kite for power generation, J. Guid. Control Dyn. 37 (5) (2014) 1426–1436. doi:10.2514/1.G000545.

[11] S. G. C. de Groot, J. Breukels, R. Schmehl, W. J. Ockels, Modeling kite flight dynamics using a multibody reduction approach, J. Guid. Control Dyn. 34 (6) (2011) 1671–1682. doi:10.2514/1.52686.

[12] U. Fechner, R. van der Vlugt, E. Schreuder, R. Schmehl, Dynamic model of a pumping kite power system, Renew. EnergyarXiv:1406.6218, doi:10.1016/j.renene.2015.04.028.

[13] R. van der Vlugt, J. Peschel, R. Schmehl, Design and experimental characterization of a pumping kite power system, in: U. Ahrens, M. Diehl, R. Schmehl (Eds.), Airborne Wind Energy, Green Energy and Technology, Springer, Berlin Heidelberg, 2013, Ch. 23, pp. 403–425. doi:10.1007/978-3-642-39965-7_23.

[14] KiteGen Stem Presentation, KiteGen Research S.r.l. Video retrieved on 2016-11-28 (2009).
URL https://www.youtube.com/watch?v=3fINSbhLhAg

[15] R. H. Dawson, Kite Turning, Master's thesis, Univesity of Canterbury, New Zealand (2011).

[16] M. Diehl, Real-time optimization for large scale nonlinear processes, Ph.D. thesis, Heidelberg University (2001).
URL http://www.ub.uni-heidelberg.de/archiv/1659

[17] B. Houska, M. Diehl, Optimal control for power generating kites, in: Proc. 9th European Control Conf., Kos, Greece, 2007, pp. 3560–3567.

[18] G. Sánchez-Arriaga, Dynamics and control of single line kites, Aeronaut. J. 110 (1111) (2006) 615–621. doi:10.1017/S0001924000001470.

[19] E. J. Terink, J. Breukels, R. Schmehl, W. J. Ockels, Flight dynamics and stability of a tethered inflatable kiteplane, J. Aircraft 48 (2) (2011) 503–513. doi:10.2514/1.C031108.

[20] S. Gros, M. Diehl, Modeling of airborne wind energy systems in natural coordinates, in: U. Ahrens, M. Diehl, R. Schmehl (Eds.), Airborne Wind Energy, Green Energy and Technology, Springer, Berlin Heidelberg, 2013, Ch. 10, pp. 181–203. doi:10.1007/978-3-642-39965-7_10.

[21] L. Salord Losantos, G. Sánchez-Arriaga, Flight dynamics and stability of kites in steady and unsteady wind conditions, J. Aircraft 52 (2) (2015) 660–666. doi:10.2514/1.C032825.

[22] J. Alonso-Pardo, G. Sánchez-Arriaga, Kite model with bridle control for wind-power generation, J. Aircraft 52 (3) (2015) 917–923. doi:10.2514/1.C033283.

[23] B. Etkin, Dynamics of flight: stability and control, John Wiley & Sons Australia, Limited, 1982.
URL https://books.google.es/books?id=4n5TAAAAMAAJ

[24] P. Williams, B. Lansdorp, R.Ruiterkamp, W. Ockels, Modeling, simulation, and testing of surf kites for power generation, AIAA Paper 2008-6693 (2008).

[25] G.-B. Hur, Identification of powered parafoil-vehicle dynamics from modelling and flight test data, Ph.D. thesis, Texas A & M Univ. (2005).

[26] M. Lara, J. Peláez, On the numerical continuation of periodic orbits. an intrinsic, 3-dimensional, differential, predictor-corrector algorithm, Astron. Astrophys. 389 (2002) 692–701. doi:10.1051/0004-6361:20020598.